Mechanism of bacterial outer membrane exchange revealed by quantitative microscopy

Elias J. Topo[1], Carolina Basurto De Santiago[1], Pengbo Cao[2,3], Daniel Wall[2#] and Beiyan Nan[1#]

[1]Department of Biology, Texas A&M University, College Station TX 77843, USA

[2]Department of Molecular Biology, University of Wyoming, Laramie, WY 82071, USA

[3]Present address: School of Medicine, Westlake University, Hangzhou, China

Running title: OME molecular mechanism

#Address correspondence to Daniel Wall, dwall2@uwyo.edu; Beiyan Nan bnan@tamu.edu

Keywords: *Myxococcus xanthus*, single molecule tracking, cell surface protein, outer membrane exchange, kin recognition, membrane fusion, fusogen

Abstract

Kin recognition, the ability to distinguish self from nonself at the cellular level is critical to multicellular life. *Myxococcus xanthus* is a multicellular bacterium that cooperates among genetically-related cells and reduces exploitation by nonkin through outer membrane exchange (OME) of common goods and toxins. The polymorphic cell surface receptor called TraA and its partner protein TraB mediate kin recognition by OME, but its molecular mechanism remains unknown. Here we used quantitative microscopy techniques to characterize the stoichiometry of the intracellular TraAB complexes and the intercellular TraA-TraA interactions. We visualized the OME of single protein particles between cells and revealed that OME depends on the free diffusion of outer membrane (OM) contents. Based on the predicted structures, we propose a model that TraAB overcomes the repulsion between OMs by stressing the membranes and reducing the contact area, analogous to the eukaryotic soluble N-ethylmaleimide-sensitive factor attachment protein receptors (SNAREs), which mediate plasma membrane fusion. Our working model provides a novel pathway that leads to an underlying conserved mechanism for membrane fusion that is a foundation process for multicellularity.

39 **Introduction**

40 The ability to distinguish self from nonself at the cellular level is critical to multicellular life.
41 This process ensures that highly related or clonal cells interact cooperatively while excluding
42 unrelated cells, which are often detrimental to multicellularity. For organisms that build
43 multicellularity by aggregating cells from their environment, self/nonself-recognition, or kin
44 recognition, is of paramount importance for coalescing a cooperative collective.

45 Myxobacteria are a group of aggregative multicellular organisms that possess
46 known systems for distinguishing relatedness at the genus and species levels.
47 Specifically, *Myxococcus xanthus* uses the type VI secretion system (T6SS) and outer
48 membrane exchange (OME) for this purpose (Vassallo & Wall, 2019, Vassallo *et al.*, 2020,
49 Gong *et al.*, 2018). The T6SS is used by many Gram-negative bacteria for various types of
50 social conflicts and virulence and is relatively well understood (Cherrak *et al.*, 2019). In
51 contrast, OME is restricted to myxobacteria and is not as well studied.

52 OME self-recognition occurs through homotypic binding between adjacent cells,
53 mediated by their polymorphic cell surface receptor called TraA and its operonic partner,
54 TraB (Pathak *et al.*, 2013, Cao & Wall, 2017). Following cell-cell recognition, TraAB
55 catalyzes OME, which involves the bidirectional transfer of different outer membrane
56 proteins (OMPs) and lipids between cells (Nudleman *et al.*, 2005, Pathak *et al.*, 2012b,
57 Wall, 2014a). This process is thought to occur by transient outer membrane (OM) fusion,

58 where TraAB acts as a fusogen on each interacting cell (Cao *et al.*, 2015, Cao & Wall, 2019).
59 The TraA protein contains a signal peptide (SP), a variable domain (VD) responsible for
60 recognition specificity, a cysteine-rich repeat region that likely functions as a presentation
61 stalk for the VD, and a MYXO-CTERM sorting tag that is likely lipidated to anchor it to
62 the cell surface (Sah *et al.*, 2020, Guo *et al.*, 2025). TraB contains an SP, an OM β-barrel,
63 and an OmpA cell-wall-binding domain. Forward genetic screens suggest that TraAB are
64 the only proteins required for OME (Dey & Wall, 2014).

65 OME serves two broad functions: mediating cooperation and discriminating
66 between cells (Sah & Wall, 2020). For cooperation, OME can rescue genetic defects in
67 recipient cells by transferring a wild-type protein from donor cells (Hodgkin & Kaiser,
68 1977, Pathak *et al.*, 2012b). OME can also rescue lethal OM defects by transferring
69 lipopolysaccharides (LPS) from healthy donors (Vassallo & Wall, 2016). Additionally,
70 when individual cells coalesce into tissue-like assemblages, genetically identical cells can
71 have distinct life histories that result in different adaptations depending on their age
72 and/or microenvironment exposures. Here, OME facilitates the transition to
73 homogeneous and synchronized cell populations with respect to their OM components,
74 thus facilitating cooperation. Finally, adaptive traits suited to particular environments
75 can be transferred to naïve siblings via OME (Subedi *et al.*, 2024), thus preparing or
76 adapting them against future stresses.

77 OME also functions to discriminate against distant kin. This occurs by the exchange
78 of dozens of polymorphic lipoprotein toxins that belong to six different families (Dey *et*
79 *al.*, 2016, Vassallo *et al.*, 2017, Vassallo & Wall, 2019, Weltzer *et al.*, 2025). Therefore, when
80 partnering cells are clonal, they are not intoxicated because they express a cognate set of
81 immunity proteins, which themselves are not exchanged. In contrast, when nonclonal
82 cells fortuitously possess compatible TraA receptors, a second discrimination step occurs,
83 wherein cells are reciprocally poisoned because they lack a complete set of immunity
84 proteins. These steps result in an extremely high level of specificity for self-recognition,
85 ensuring that highly related collectives form for multicellular functions, such as fruiting
86 body development.

87 Membrane fusion plays a central role in many biological processes in eukaryotic
88 cells, but in bacteria there are few examples and little is known. Here, we sought to
89 address key questions about the molecular mechanism of OME. First, we sought to
90 understand the nature of TraAB multimeric complexes that form upon cell-cell contact
91 and OME engagement. Following the coalescing of receptors, these complexes are readily
92 visualized as foci when using functional fluorescent protein fusions to TraA or TraB.
93 However, the stoichiometry of the intercellular TraA junction and the intracellular TraAB
94 complexes remains unknown. Second, since client OME cargos do not contain specificity
95 factors for transfer, but must be diffusible in a fluid OM, we aimed to measure the fluidity
96 of *M. xanthus* OM. Third, do these foci junctions serve as conduits for the transfer of client

97 proteins, and what trajectories do these proteins follow upon OME? Using
98 photobleaching and single molecule tracking techniques, we addressed these questions
99 and proposed an updated model of OME in myxobacteria.

100 **Results**

101 **Stoichiometry of the intercellular TraA foci**

102 TraAB are thought to function as fusogens to catalyze OM fusion between cells. By using
103 fluorescent fusion reporters to TraA or TraB they were found to coalesce into foci aggregates
104 upon cell contact (Cao & Wall, 2019). Here we sought to address (i) how many TraA
105 molecules are present in these foci? (ii) Do all the TraA foci contain the same stoichiometry,
106 and (iii) do interacting cells contribute the same number of TraA proteins in each focus? To
107 answer these questions, we used a functional monomeric super folder green fluorescent
108 protein (GFP)-labeled TraA (TraA-GFP) expressed from the heterologous *pilA* promoter and
109 placed it in a Δ*traA* strain (Cao & Wall, 2019). We mixed this strain with wild-type (unlabeled)
110 cells at a 1:2 ratio and spotted the cell mixture on a 1.5% agar surface. As reported (Cao &
111 Wall, 2019), TraA-GFP distributed uniformly throughout the OM of isolated cells. However,
112 upon cell-cell contact, we observed two types of TraA foci at contact junctions, bright foci
113 occurred between two labeled cells and dim foci between labeled and unlabeled cells (**Fig.**
114 **1A**).

115 The intensities of TraA-GFP foci appeared heterogeneous, regardless of whether only
116 one or both cells were labeled (**Fig. 1A**), suggesting that individual TraA foci do not adopt
117 the same stoichiometry. We then subjected the TraA-GFP foci to photobleaching using a 488-
118 nm laser (0.5 kW/cm^2) and monitored the decrease of fluorescent signals continuously at 67
119 Hz (15 ms/frame). The intensity of these foci decreased in discrete steps of the same size,

120 which we define as Δ*i* that reflected the photobleach of one GFP molecule (**Fig. 1B**).
121 Occasionally we saw larger bleach steps where the intensity decreased by 2Δ*i*, indicating that
122 two molecules were bleached simultaneously (**Fig. 1B**). Therefore, the number of Δ*i* bleach
123 steps equals the number of TraA-GFP molecules within the focus (**Fig. 1B, Movie S1**).

124 Consistent with the variation of their fluorescent intensities, the 174 foci between labeled
125 cells lost fluorescence after 2 to 10 steps of photobleaching, indicating that these foci
126 contained 2 to 10 TraA-GFP molecules (**Fig. 1B, Movie S1**). The numbers of TraA-GFP
127 molecules in each focus displayed a typical Gaussian distribution. Importantly, we never
128 observed any foci that was bleached in a single step of Δ*i*, suggesting that at least one TraA
129 molecule in each juxtaposed cell is required to establish the intercellular junction. This result
130 was consistent with the observation that TraA-GFP expressing cells cannot form TraA foci
131 when it contacts a Δ*traA* cell (Cao & Wall, 2019). In addition, 46% of these foci contained odd
132 numbers of TraA molecules, indicating that the formation of these foci does not necessarily
133 require the same number of TraA molecules from two juxtaposed cells.

134 Among the 204 foci found between labeled and unlabeled cells, the number of TraA-GFP
135 molecules also showed a nearly symmetric distribution between 1 and 6, roughly half as
136 many as detected in the foci between two labeled cells (**Fig. 1C**). The detection of foci that
137 contained only one TraA-GFP molecule further confirmed that a single TraA molecule from
138 each contacting cell was sufficient to establish an intercellular TraA junction. Taken together,

139 TraA foci at cell-cell contact sites contain molecules from both juxtaposed cells where each

140 cell may contribute different numbers of TraA molecules.

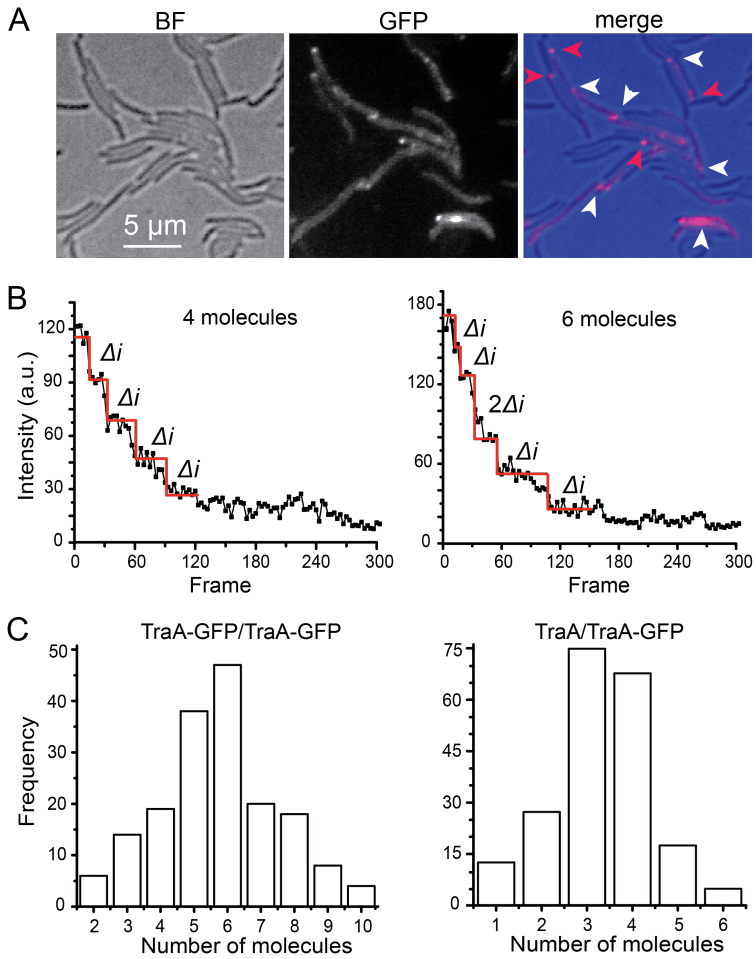

Fig. 1. TraA forms heterogeneous foci at cell-cell contact sites. **A)** Representative images of the TraA-GFP foci. The Δ*traA traA-gfp* cells were mixed with wild-type (unlabeled) at a 1:2 ratio. White arrows indicate foci formed between labeled cells and red arrows between labeled and unlabeled cells. **B)** Examples of the photobleached foci that contain 4 and 6 TraA-GFP molecules, respectively. The decrease step of fluorescence corresponds to one GFP molecule being photobleached (*Δi*). **C)** The number of TraA-GFP molecules in each focus between labeled cells (left, n = 174) and between labeled and unlabeled ones (right, n = 204).

141

142 **TraA and TraB form complexes at a 1:1 ratio**

143 TraA requires its partner OMP TraB to form functional complexes (Pathak *et al.*, 2012a, Cao

144 & Wall, 2017). Although TraB does not play a specificity role in kin recognition, TraA and

145 TraB colocalize into the foci between adjacent cells in an interdependent manner, suggesting
146 that these proteins form intracellular complexes (Cao & Wall, 2019). However, the
147 stoichiometry of these complexes is unknown. To address this question, we used a strain that
148 expressed both TraA-mCherry and TraB-GFP and photobleached both mCherry and GFP
149 simultaneously using Hamamatsu W-VIEW GEMINI™ beam-splitter. TraA and TraB
150 colocalized in the foci between juxtaposed cells (**Fig. 2A**). To simplify analysis, we recorded
151 the photobleach of both fluorophores at 5 Hz (200 ms/frame, **Movie S2**). Using this method,
152 we found that the numbers of TraA-mCherry in each focus varied between 2 and 12 in the 59
153 analyzed foci (**Fig. 2B**), consistent with the photobleach result from TraA-GFP (**Fig. 1C**).
154 Importantly, the TraB-GFP molecules displayed a similar distribution pattern (**Fig. 2B**). We
155 further investigated the correlation between TraA and TraB in each focus and found that each
156 TraA molecule correlated with 0.98 TraB molecules, indicating that TraA and TraB form
157 complexes at a 1:1 ratio (**Fig. 2C**).
158

159 ***M. xanthus* contains a highly fluid OM**

160 The model bacterium *Escherichia coli* has a rigid OM (Rojas *et al.*, 2018, Sun *et al.*, 2022). As a
161 consequence, the lateral mobility of OMPs is restricted due to the formation of large OMP
162 islands and the selective presence of bulky LPS molecules in the outer leaflet (Rassam *et al.*,
163 2015, Benn *et al.*, 2021). In contrast, *M. xanthus* cells are flexible and can exchange a broad
164 range of OM molecules efficiently, including OMPs, LPS, and dyes (Ducret *et al.*, 2013,

165 Vassallo *et al.*, 2015, Pathak *et al.*, 2012a). Since heterologous proteins, like a lipidated GFP,

166 are readily exchanged as cargos, OME does not require other *cis* specificity sequences for

167 transfer. Instead, these cargos are likely transferred between cells by diffusion, which

168 requires a fluid OM (Cao & Wall, 2020, Cao & Wall, 2019). However, the fluidity of *M. xanthus*

169 OM has not been measured.

170 To measure membrane fluidity, we used the diffusion rate of OMPs as a proxy. Here, we

171 used a lipoprotein where a type II signal sequence was fused to the fluorescent protein

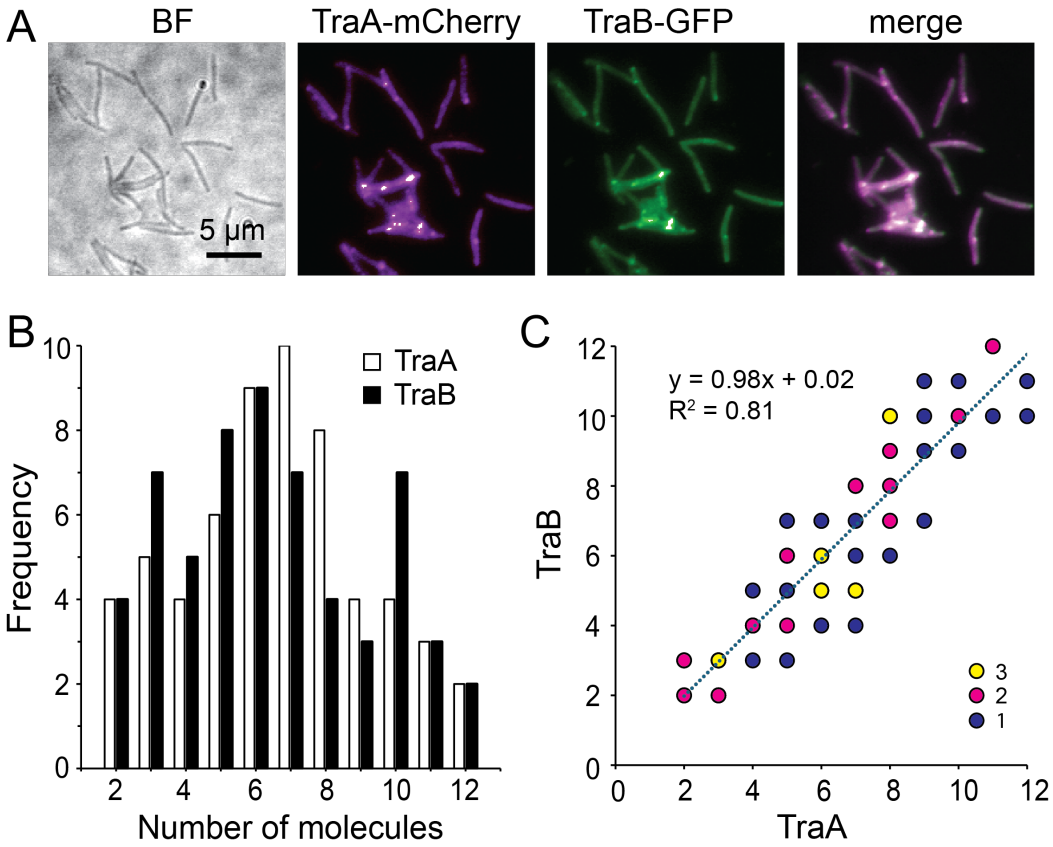

Fig. 2. TraA and TraB form intracellular complexes at a 1:1 ratio. **A)** TraA-mCherry and TraB-GFP colocalize in the foci between adjacent cells. **B)** From 59 foci analyzed, the number of TraA and TraB proteins in each focus show similar distribution patterns. **C)** The correlation between the numbers of TraA and TraB in individual foci suggests a 1:1 ratio in the intracellular TraAB complexes. In each focus, the number of TraB is plotted against that of TraA. The numbers of foci that have the same TraA:TraB ratio are indicated by color.

172 mCherry and expressed as a recombinant SSOM-mCherry reporter in *M. xanthus*. This simple
173 lipoprotein tag was sufficient for the OM localization of mCherry and enabled it to be
174 transferred by OME (Wei *et al.*, 2011). We reengineered this strain by replacing mCherry with
175 the photoactivatable mCherry (PAmCherry). mCherry and PAmCherry are of the same size
176 and share 95.8% protein sequence identity. We used a 405-nm excitation laser (0.2 kW/cm^2,
177 0.1 s) to activate the fluorescence of a few labeled SSOM-PAmCherry particles randomly (here
178 we refer isolated fluorescence spots as single particles rather than "single molecules" because
179 each spot could contain more than one molecule, albeit only the fluorescence of one molecule
180 was activated). We imaged the activated particles at 67 Hz using a 561-nm laser with total
181 internal reflection fluorescence (TIRF) microscopy (Fu *et al.*, 2018, Nan *et al.*, 2015, Nan *et al.*,
182 2013). Using this setting, only a thin section of each cell close to the coverslip was illuminated,
183 which included the cell surface. As free SSOM-PAmCherry particles diffuse extremely fast in
184 the cytoplasm, entering and exiting the focal plane frequently, they usually appear as blurry
185 objects that cannot be followed close to the cell surface (Fu *et al.*, 2018, Zhang *et al.*, 2023b).
186 For this reason, the noise from the SSOM-PAmCherry molecules that were not yet inserted into
187 the OM was negligible. To exclude the potential influence of cell-cell contact, we only
188 analyzed the dynamics of SSOM-PAmCherry particles in isolated cells. Using single particle
189 tracking photo-activated localization microscopy (sptPALM), we identified 1,518 fluorescent
190 particles that remained in focus for 4 - 12 frames (0.4 - 1.2 s) and plotted their mean squared
191 displacements (MSDs) against time lag (Δt). The linear relationship between MSD and Δt

192 indicated that single SS_{OM}-PAmCherry particles moved by typical diffusion (**Fig. 3A, B,**
193 **Movie S3**). The diffusion coefficient (*D*) of the entire population was 0.19 ± 0.04 μm²/s (n =
194 1518, **Fig. 3C**), in the same order of magnitude as the unrestricted diffusion of proteins in the
195 cytoplasm, IM, and periplasm in other bacteria, such as *E. coli* and *Bacillus subtilis* (Parry *et*
196 *al.*, 2014, Lucena *et al.*, 2018, Tran *et al.*, 2024). Importantly, the diffusion of SS_{OM}-PAmCherry
197 was about 10-fold faster than the restricted diffusion of *M. xanthus* proteins in the IM and
198 periplasm (Fu *et al.*, 2018, Nan *et al.*, 2013, Zhang *et al.*, 2023b, Ramirez Carbo *et al.*, 2024),
199 suggesting that SS_{OM}-PAmCherry diffuses with little restriction in the OM.

200 The bacterial IM is known to be fluid, where many proteins diffuse freely (Lucena *et al.*,
201 2018). As a control, we engineered a strain that localizes mCherry to the IM (SS_{IM}-mCherry)
202 (Wei *et al.*, 2011) by replacing mCherry with PAmCherry. As expected, we found that the
203 recombinant SS_{IM}-PAmCherry also diffused freely, with a *D* value of 0.22 ± 0.02 μm²/s (n =
204 2848), close to that of SS_{OM}-PAmCherry (**Fig. 3, Move S4**). Taken together, like the IM, the
205 OM of *M. xanthus* is highly fluid and such fluidity provides the mechanistic foundation for
206 OME.

207

208 **OME depends on the diffusion of OM components**

209 OME between *M. xanthus* cells has been imaged in real-time (Ducret *et al.*, 2013, Cao & Wall,
210 2019). However, the mechanism of OME is not fully understood. For instance, does OME
211 depend on the diffusion of the client cargos, or the exchange of large OM fragments? To

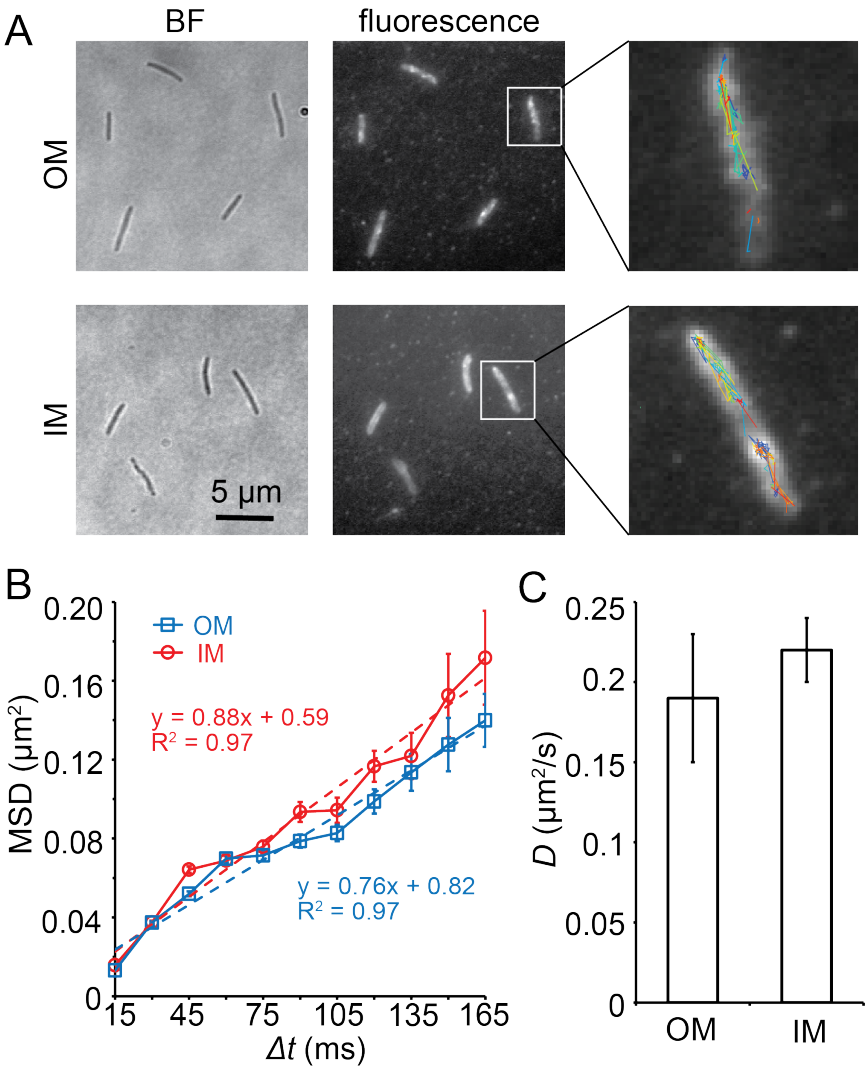

Fig. 3. SSOM-PAmCherry diffuses rapidly in the *M. xanthus* OM. **A)** Single PAmCherry particles diffuse freely in both the OM and IM. The overall distribution of SSOM- and SSIM-PAmCherry is displayed using the composite of 100 consecutive frames taken at 15-ms intervals. Single-particle trajectories of PAmCherry were generated from the same frames. Individual trajectories are distinguished by colors. **B)** The linear relationship between MSD and Δt indicates that PAmCherry diffuses freely in both OM (n = 1518) and IM (n = 2848). **C)** PAmCherry shows similar diffusion coefficients in OM (n = 1518) and IM (n = 2848).

212 investigate the dynamics and trajectories of client proteins during OME, we visualized and

213 tracked single SSOM-PAmCherry particles. If OME requires diffusion, then SSOM-PAmCherry

214 particles should quickly travel between cells. Alternatively, if cells exchange bulk OM

215 fragments, the exchange of SS$_{OM}$-PAmCherry particles should be slow due to the size of such
216 fragments.

217 To test these possibilities, we used cells that expressed SS$_{OM}$-PAmCherry as donors and
218 Δ*traA* P$_{pilA}$-*traA-gfp* cells as recipients. We mixed these strains at a 1:1 ratio on a 1.5% agar
219 surface. To increase the chance of capturing OME, we first exposed cells under the 405-nm
220 laser for 2 s, where the majority of PAmCherry was photoactivated (Fu *et al.*, 2018). We then
221 excited the fluorescence of PAmCherry and GFP using the 561-nm and 488-nm lasers,
222 respectively, and imaged both channels simultaneously using the beam-splitter. As SS$_{OM}$-
223 PAmCherry particles moved rapidly (**Fig. 3**), we had to track their movements at a high frame
224 rate (67 Hz). For this reason, we could only image each field for a few seconds before the
225 reporters' photobleach (**Fig. 1**). In these short time windows, OME was rarely visualized.
226 Nevertheless, we captured OME of 39 SS$_{OM}$-PAmCherry particles (**Fig. 4A-C, Movie S5-S7**).
227 Their MSD showed a linear relationship with Δt, with a D value of 0.21 ± 0.07 μm^2/s (n = 39),
228 close to the intracellular diffusion rate of SS$_{OM}$-PAmCherry particles. These results indicate
229 that cell-cell contact does not hinder OMP diffusion, and that OME depends on the diffusion
230 of OM content, rather than the transfer of large OM fragments (**Fig. 4D**).

231 By closely tracking particle trajectories during OME, we found six cases where SS$_{OM}$-
232 PAmCherry particles transferred to recipient cells and then returned to the donors (**Fig. 4A,**
233 **Movie S5**). This observation was consistent with OME occurring bidirectional, where
234 'recipients' can also act as donors. Strikingly, we identified five SS$_{OM}$-PAmCherry particles

being transferred between more than two cells. For instance, the particle shown in **Fig. 4B** and **Movie S6** passed three cell-cell boundaries. Thus, through TraAB-mediated kin

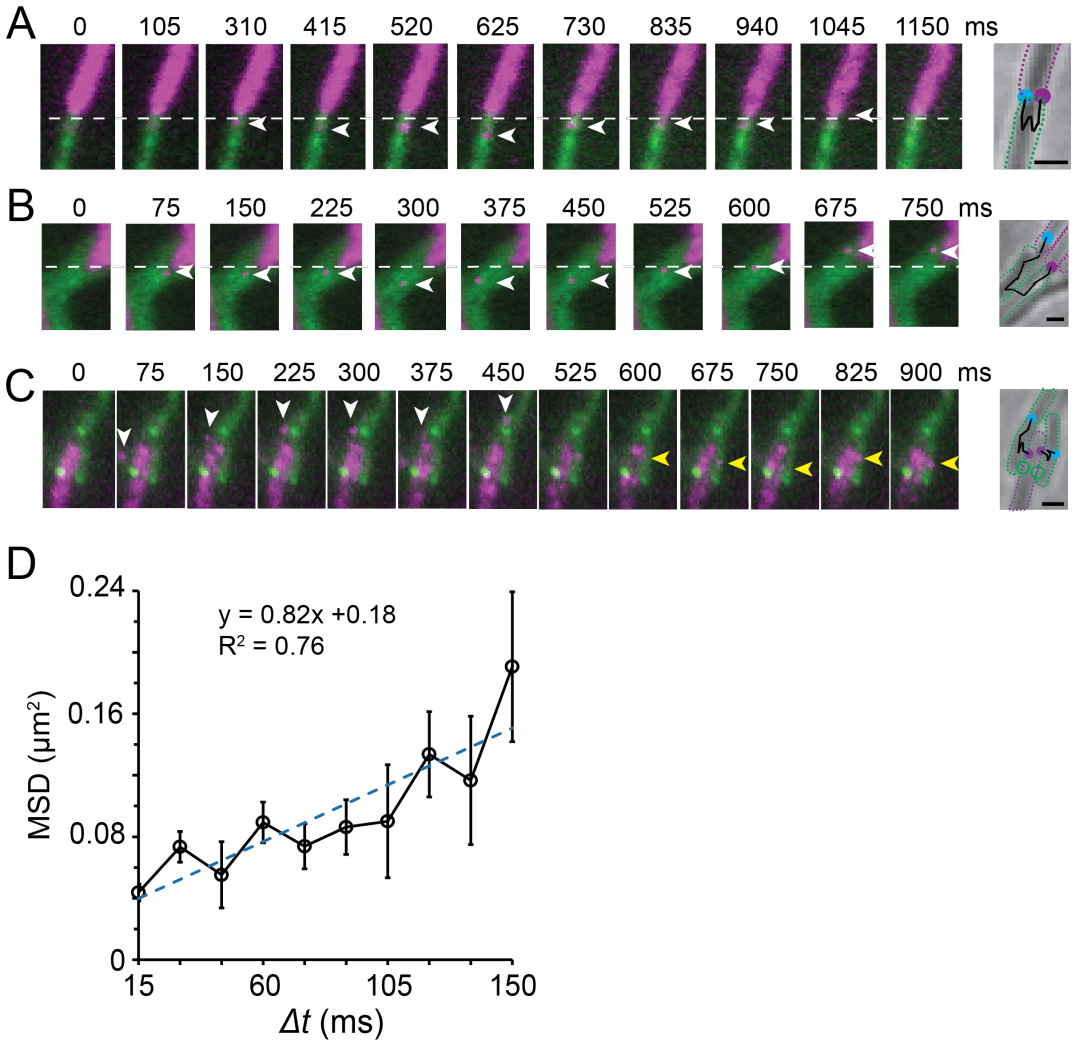

Fig. 4. OME requires cargo diffusion. **A - C)** Example trajectories of single SSOM-PAmCherry particles during OME. The cells expressing SSOM-PAmCherry (magenta) and TraA-GFP (green) were mixed at a 1:1 ratio. Arrows point to the exchanged particles. On the right side of each time-lapse series, the outlines of the donors and recipients are marked with purple and green dotted lines, respectively. The trajectories of particles are marked with black segmented lines. Their start and end positions are marked with purple and blue circles, respectively. Scale bars, 1 μm. The uncropped videos for these OME events are Movies S5, S6, and S7. In A) and B), the initial positions of the donor cell poles are marked with white dashed lines in the time-lapse images. In C), the positions of two TraA foci are marked with green circles on the right panel. **D)** The linear relationship between MSD and Δt of the 39 transferred particles indicates they diffuse freely during OME.

237 recognition, client proteins can be serially transferred between clonemates to achieve long-
238 range OME among multiple adjacent cells.
239
240 **TraA foci do not correlate as the channels for OME**
241 Here we sought to investigate the role of TraAB complexes in OME and if they serve as
242 transfer portals. To answer these questions, we followed the trajectories of single-particle
243 OME events between cells that made lateral contacts. Such juxtaposed side-by-side cells
244 frequently formed multiple TraA foci, which allowed us to ask whether these foci correlated
245 as the sites where SSOM-PAmCherry particles crossed the cell-cell boundaries. However, out
246 of the seven SSOM-PAmCherry particles that transferred through lateral side-by-side cells,

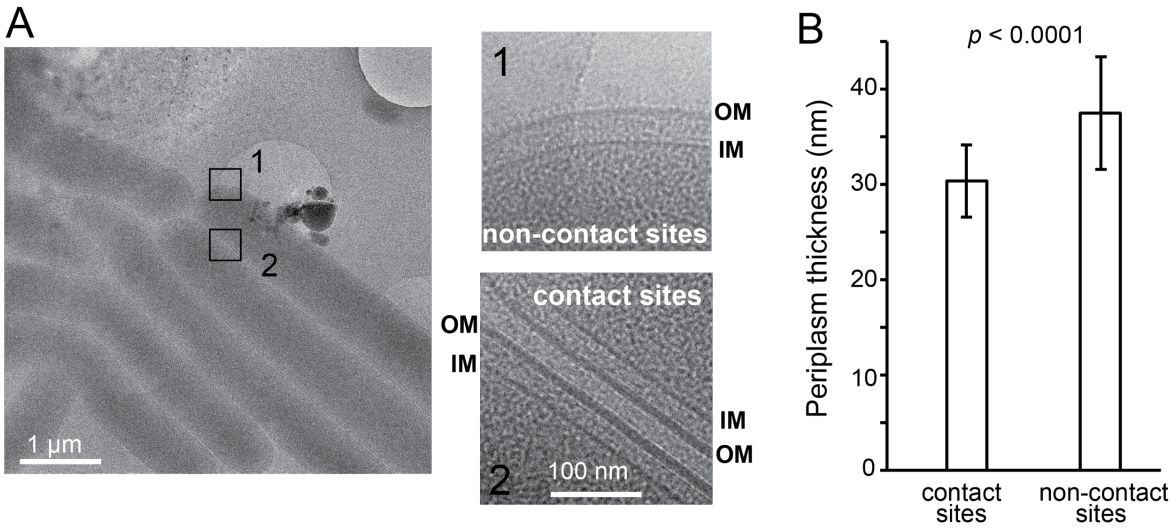

Fig. 5. OMs in juxtapose cells are stressed at cell-cell contact sites. **A)** cryo-EM images show that in the same cell, the OM is relaxed at non-contact sites while stressed at cell-cell contact sites. **B)** The OM stress compresses the periplasms at cell-cell contact sites. Periplasmic thickness was measured as the distance between the centers of the OM and IM densities from seven contacting cell pairs, 30 measurements/pair. The *p* value was calculated using a one-way ANOVA test between two unweighted, independent samples.

247 none of them passed through the TraA foci (**Fig. 4C, Movie S7**). These observations strongly
248 suggest that TraAB complexes do not form transfer channels for OME.
249
250 **Repulsive interaction between cells obstructs OME**
251 Cells lacking functional TraAB or expressing incompatible TraA variants make close contacts
252 but do not transfer their OM contents (Wei *et al.*, 2011). Why are physical cell-cell contacts
253 alone insufficient for OM fusion? To answer this question, we investigate cell-cell contacts
254 using cryogenic electron microscopy (cryoEM). To avoid the potential interference from
255 extracellular polysaccharides (EPS), we grew *pilA*$^-$ cells that do not produce EPS (Yang *et al.*,
256 2010) in liquid culture, concentrated cells by centrifugation, and captured micrographs of *M.*
257 *xanthus* cells in close contact, where we found cell groups of various sizes. As OME does not
258 occur in liquid, these cells displayed the character of OMs before fusion (**Fig. 5A**). Analyzing
259 these micrographs, we found two remarkable features. First, regardless of group size, direct
260 touch between OMs was not observed (**Fig. 5A**). The distances between the centers of the OM
261 densities at side-to-side cell contact sites varied between 20.4 nm and 34.5 nm, with an
262 average distance of 28.8 ± 3.4 nm (measure from three pairs of cells, 30 measurements/pair).
263 Therefore, the interaction between the OMs is under the regime of electrostatic repulsion and
264 beyond the range of van der Waals attraction, 0.3 – 0.5 nm (Batsanov, 2001). Such repulsion
265 is comparable to the one between liposomes that prevents their fusion in aqueous media
266 (Jahn *et al.*, 2024). Hence juxtaposed cells are always separated by a thin water layer and the

267 repulsion between cells physically obstructs OM fusion. Second, the periplasms appeared
268 compressed at cell-cell contact sites (**Fig. 5A**). Strikingly, in the cells that contact others only
269 on one side, while the contact sides displayed compressed periplasms with the thickness (the
270 distance between the centers of the OM and IM densities) of 30.4 ± 3.8 nm (measured from
271 seven pairs of cells, 30 measurements/pair, **Fig. 5B**), the non-contact sides retained relaxed
272 periplasms of 37.5 ± 5.9 nm thickness (measured from the same seven pairs of cells, 30
273 measurements/pair, **Fig. 5B**). This result shows that cell-cell contacts increase the surface
274 tension of OMs. Therefore, similar to plasma membranes that do not fuse spontaneously
275 (Rand & Parsegian, 1984), repulsion must be overcome to bring OMs closer, which poses a
276 major energy barrier in OM fusion.
277
278 **Molecular mechanism for TraAB-mediated OM fusion**
279 To understand how one intercellular TraAB-TraAB dimer induces OM fusion, we used
280 AlphaFold (Jumper *et al.*, 2021) to predict the structures of TraA and TraB. Using the
281 sequences of the processed proteins (amino acids 37 – 684 for TraA, excluding its SP and the
282 cleaved MYXO-CTERM (Sah *et al.*, 2020) and 23 – 543 for TraB, excluding its SP), AlphaFold
283 generated highly-confident structure models for both proteins in their monomeric states (**Fig.
284 6A**). TraA monomer forms a dumbbell-like structure where the N-terminal VD, containing
285 at least eight β-sheets, forms the first dumbbell head. The shaft is an extended cysteine-rich
286 region, which makes a 180° turn at the end, forming the second dumbbell head (**Fig. 6A**). This

287 region, containing more than 70 cysteines, forms at least eight β-hairpins that each consists
288 of two antiparallel β-strand connected by a short loop (**Fig. 6A**). We predict that at cell
289 surfaces where thiol groups are oxidized, this region is stiffened by dozens of disulfide
290 bonds. Consistent with a previous finding that the VD determines the recognition between
291 TraA variants (Cao & Wall, 2017), the AlphaFold structure showed two TraA molecules
292 interacting through their VDs, forming a head-to-head dimer (**Fig. 6A**). Strikingly, the length
293 of a TraA dimer is ~ 28 nm, matching the distance between OMs in tightly packed cell groups.

294 The TraB protein consists of a N-terminal β-barrel and a C-terminal OmpA-like domain,
295 linked together by short thrombospondin type 3 (TSP3) repeats predicted to bind calcium
296 (Dai *et al.*, 2017) (**Fig. 6A**). Consistent with their colocalization and 1:1 stoichiometry (**Fig. 2**),
297 AlphaFold also predicted a 1:1 TraAB complex in which the second dumbbell head of TraA
298 is positioned on top of the β-barrel in TraB (**Fig. 6A**). However, AlphaFold did not predict
299 significant conformational changes in TraA after its dimerization and interaction with TraB
300 (**Fig. 6A**). Nevertheless, because TraB is diffusive in isolated cells but colocalizes with TraA
301 in the relatively stationary intercellular foci (Cao & Wall, 2019), TraA dimerization could
302 introduce conformational changes in TraB, which likely promotes binding to peptidoglycan
303 (PG) and thus restrains the diffusion of the TraAB-TraAB dimers.

304 Based on these predictions, we propose a bulge-and-slide working model for TraAB-
305 mediated OM fusion that has similarities to the eukaryotic soluble N-ethylmaleimide-
306 sensitive factor attachment protein receptors (SNAREs) that mediate vesicle membrane

307 fusion. To facilitate fusion, membranes must be brought close together, and one way to do
308 this is to minimize their contact area. Eukaryotes utilize membrane-anchored SNARE
309 proteins to establish point-to-point contacts that perturb the bilayer structure and thereby
310 lower the energy barrier for fusion. Once SNARE proteins from juxtaposed membranes
311 establish contact, the SNARE complex tighten their coiled-coil domains into bundles,
312 mimicking a zipper that pulls the membranes together until they merge (Jahn *et al.*, 2024)(**Fig.**
313 **6D**). Through this mechanism, one to three SNARE complexes are sufficient to catalyze
314 membrane fusion (Jahn *et al.*, 2024, Sinha *et al.*, 2011, Shi *et al.*, 2012, van den Bogaart *et al.*,
315 2010). Similarly, we propose that when two cells that express compatible TraA variants
316 approach each other, TraA molecules establish point-to-point contacts between them.
317 Diffusing TraA molecules can then form intercellular dimers in a head-to-head orientation,
318 which is consistent with TraA foci formation between topologically opposed OMs. The
319 TraAB complexes could anchor to PG through the OmpA domain in TraB and thus forms
320 relatively stationary junction foci like SNARE complexes (**Fig. 6B**). While the TraA molecules
321 in a dimer are not likely to form SNARE-like zipper (**Fig. 6D**), when juxtaposed cells slide
322 against each other, the movements of cells pull the PG-anchored TraAB complexes toward
323 opposite directions that tugs on the OM and generates bulges at the base of each complex
324 (**Fig. 6B**). As the cells continue to slide, due to the rigidity of TraA, such stressed OM bulges
325 are primed for membrane fusion as they are forced into juxtaposed OMs, resulting in OM
326 fusion between cells (**Fig. 6B**). In agreement with our model, transmission electron

327 microscopy (TEM) images showed that cells overexpressing TraAB contacted each other

328 through OM bulges (Vassallo *et al.*, 2015) (**Fig. 6C**).

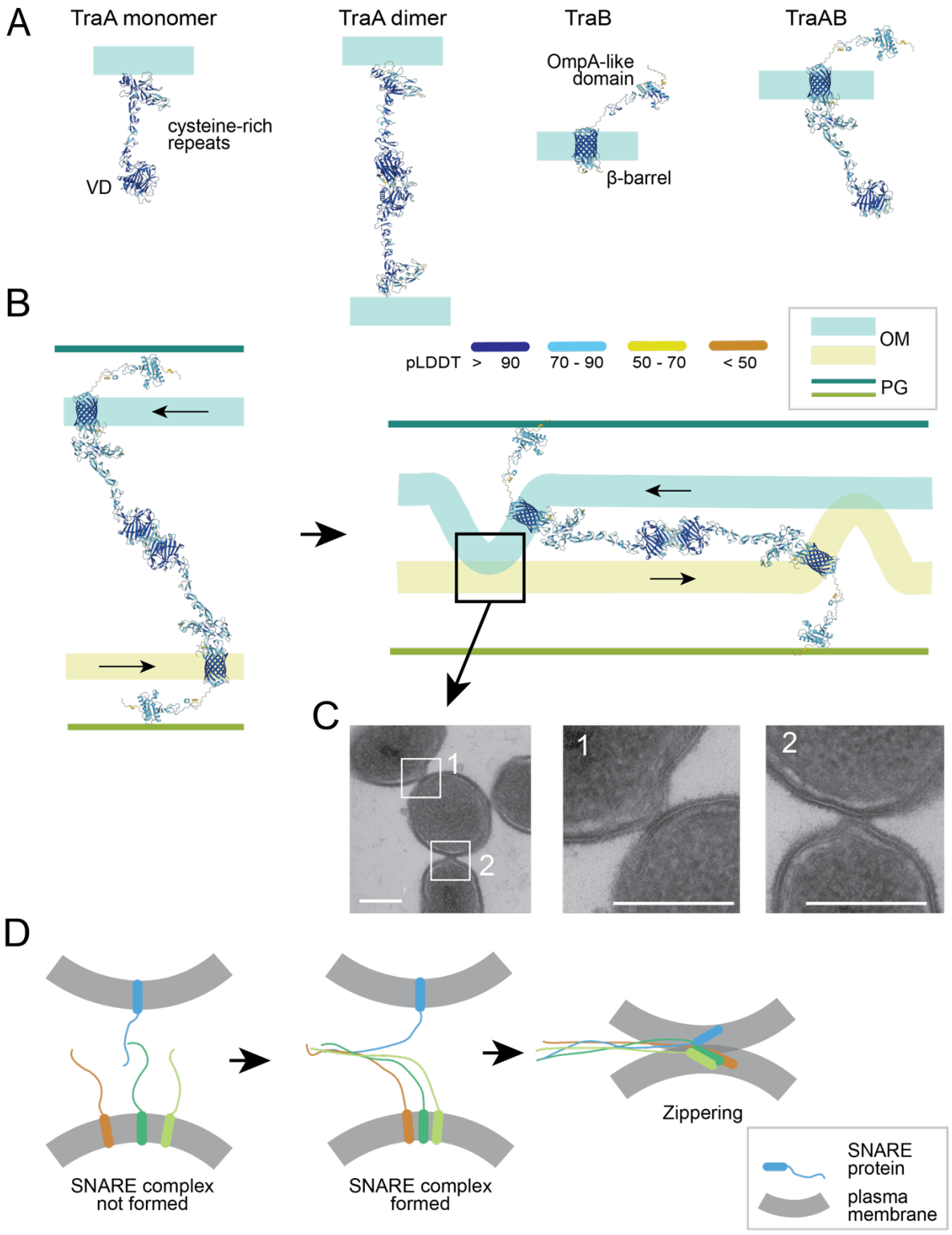

329

Fig. 6. Predicted structures of TraA, TraB, and their complexes suggest a mechanism for OM fusion comparable to the eukaryotic SNARE system. **A)** The predicted structures of TraA, TraB, and their complex. **B)** A proposed bulge-and-slide mechanism for TraAB-mediated OM fusion. When two cells with compatible TraA molecules make contact, TraA molecules form head-to-head dimers first through their VDs and TraB anchors such TraA dimers to PG. As the juxtaposed cells slide against each other, the two TraAB complexes move in opposite directions, pulling the OMs. Such mechanical stress will generate OM bulges and the continuous movements of cells will either break these bulges or bring them near the OM of the adjacent cell and thus trigger OME. Structure elements are colored according to their pLDDT (predicted local-distance difference test) scores, which indicate the prediction confidence. **C)** OM bulges - between cells that overexpress TraAB. Cyro-fixed thin section TEM images were adapted from (Vassallo *et al.*, 2015). Scale bars, 500 nm. **D)** SNARE-mediated plasma membrane fusion in eukaryotic cells. Assembly of SNAREs requires four different SNARE motifs on three or four separate proteins. Once a SNARE complex forms, the four coiled-coil domains transform into a four-helix bundle that "zips" the two membranes together.

330

331 **Discussion**

332 Multicellular organisms independently evolved from unicellular ancestors at least 25 times
333 during evolution (Grosberg & Strathmann, 2007). Myxobacteria achieve multicellularity
334 through the aggregation of single cells. While forming aggregates is relatively
335 straightforward, it is less understood how individual cells from genetically mixed
336 populations establish stable multicellular structures. For instance, how do individual cells
337 maintain cooperative cell-cell interactions while keeping cheaters at bay? Myxobacteria
338 achieve the transition from solitary, single-cell life into cooperative, multicellular tissues
339 through kin recognition and the exchange of cellular contents. Specifically, the homotypic
340 binding by their polymorphic cell surface TraA protein and its cohort protein TraB, leads to
341 OM content sharing and further discrimination against nonself by OME of polymorphic
342 toxins. To better understand the mechanism of OME we used quantitative microscopy and
343 single molecule tracking. We showed that the ratio of TraA and TraB in cell-cell junctions is
344 1:1. Moreover, we used the strong heterologous *pilA* promoter to overexpress the
345 chromosomal copy of the *traAB* operon to generate TraA foci of various stoichiometry,
346 ranging from 2 to 12. Our results confirmed that each partnering cell contributes at least one
347 TraAB complex to form a functional junction. Because the native, low expression of *traAB* is
348 sufficient for OME (Wei *et al.*, 2011), we speculate that the minimum number of TraAB
349 complexes in junctions for OME is two. Indeed, the foci that contained two TraAB complexes
350 only accounted for ~5% of all the foci we detected, which explains why such foci were hard

351 to image when TraAB were expressed with the native promoter (Cao & Wall, 2019, Vassallo
352 *et al.*, 2015). Thus, overexpression increased both the number and size of such foci. The fact
353 that TraA and TraB both peaked around six molecules in the foci suggests that when
354 overexpressed, TraB could form trimmers through its OM β-barrel domains. The wide range
355 of stoichiometry and the fact that two partnering cells do not necessarily contribute equal
356 numbers of TraAB proteins in foci junctions, suggest that TraAB do not form intercellular
357 channels with defined structures.

358 Instead, our results invoke TraAB serving as fusogens to transiently catalyze the OM
359 fusion between cells and thus allow rapid and facile cargo exchange. This model presumes
360 that the OM of *M. xanthu*s is fluid, distinct from the rigid OMs from other Gram-negative
361 bacteria such as *E. coli* (Cao & Wall, 2020). By tracking single molecules of the lipidated SS$_{OM}$-
362 PAmCherry, we showed this reporter rapidly diffuses in the OM. This analysis confirmed
363 the fluidity of *M. xanthus*, showing that diffusion rates in the OM were similar to unrestricted
364 protein diffusion rates in the cytoplasm, IM, and periplasm in other bacteria. It is unclear how
365 widely such fluid OMs exist in Gram-negative bacteria. Nevertheless, our method can be
366 easily applied to measure OM fluidity in other organisms.

367 Further support of the membrane fusion comes from tracking OME at single-particle
368 resolution. Here SS$_{OM}$-PAmCherry particles were observed to transfer from donor into
369 recipient cells at rates that are nearly identical to their diffusion rates. Strikingly, particles
370 were also observed to enter recipient cells and then return to the original donor, supporting

371 prior observations of bidirectional transfer mediated by OM fusion (Cao & Wall, 2019).
372 Finally, in tracking experiments, particles also traveled across multiple cell boundaries when
373 those cells were adjacent to one another. This result indicates that multiple cells can
374 simultaneously form fusion junctions, which are in a tissue-like state. This latter point is also
375 supported by prior findings of serial cell-cell transfer of SitA toxins (Vassallo *et al.*, 2017).

376 The last question we addressed is whether TraAB foci serve as transfer portals of OME.
377 However, our observations did not find a correlation between TraA foci and single particle
378 transfer of the SS$_{OM}$-PAmCherry reporter. Instead, transfer occurs at various sites along
379 juxtaposed cells, which are not directly correlated with TraAB foci. Given these findings, we
380 propose TraAB foci serve as sites to nucleate membrane fusion, which then proceeds bulge-
381 and-slide fashion along adjacent cells. This model is supported by cryo-EM micrographs of
382 cell cross-sections, which show regions along cell lengths that look to be involved OM fusion
383 (Vassallo *et al.*, 2015). Additionally, fluorescent time-lapse microscopy of gliding *M. xanthus*
384 cells engaged in OME shows the functional TraA-mCherry reporter dynamically coalescing
385 in a zipper-like fashion along the lengths of the interacting cells (Cao & Wall, 2019). Taken
386 together, we envision TraAB initiating an OM fusion junction that widens along the cell
387 length. Fission occurs when cell move apart from one another.

388 The outer leaflet of the *M. xanthus* OM contains LPS, consisting of the lipid A membrane
389 anchor and extended aqueous exposed polysaccharide O-antigen repeats (Perez-Burgos *et al.*,
390 2019). Additional types of lipids may also reside in their outer leaflet, but that is not fully

391 understood (Lorenzen *et al.*, 2014). Since TraAB has no known connection to the IM or
392 cytoplasmic energy sources, we propose that when cells slide against each other, the
393 mechanical force of cell movements could pull OMs outward through the rigid TraAB-TraAB
394 dimer and eventually cause OM fusion (**Fig. 6B**). Our bulge-and-slide model is similar to the
395 eukaryotic SNARE mechanism in that it overcomes the same energy barrier that obstructs
396 membrane fusion (**Fig. 6D**). However, in contrast to the SNARE complexes that require four
397 SNARE motifs from three to four proteins, the TraAB-TraAB dimer is simpler but contains
398 the same essential structural elements: the interaction domains in TraA and the membrane
399 anchor in TraA and TraB (**Fig. 6A**). Different from the SNARE complexes that pull membrane
400 together through dramatic conformational changes (**Fig. 6D**), the energy for zippering could
401 come from the sliding between cells by either motility or cell growth (**Fig. 6B**). Nevertheless,
402 we do not rule out the possibility that conformational changes in TraA also play important
403 roles in OM fusion. In this regard, a candidate conformational switch within the diverse TraA
404 family is the invariant Ser-Cys-Asn-Cys-Cys-Pro motif found in the C-terminal stalk region
405 (Cao *et al.*, 2019). Here the adjacent Cys residues may form a sterically constrained disulfide
406 bond that brakes upon tension by TraA-TraA receptors adhering as cells move in opposite
407 directions. Our model explains two important observations. First, whereas TraA and TraB do
408 not depend on each other to localize to OMs, their function as cell-cell adhesins and for the
409 formation of junction foci requires both proteins. In this case, TraA is required for kin
410 recognition and forming intercellular dimers, while TraB is essential to anchor such dimers

411 to PG and to restrain their diffusion. This latter point is supported by the finding that deletion
412 of the OmpA domain from TraB results in a mutant protein able to form foci and act as an
413 adhesion with TraA, but is not functional for OME (Balagam *et al.*, 2021). Second, OME
414 requires cell motility (Wall *et al.*, 1998, Wall & Kaiser, 1998, Wei *et al.*, 2011, Wall, 2014b). Our
415 model predicts that the relative movements pull on OMs through the rigid TraA-TraA
416 dimers, and such mechanical stress will produce pronounced OM bulges that bring OMs
417 together, while also perturbing the bilayer structure, and thereby lowering the energy barrier
418 to the point where fusion occurs spontaneously (**Fig. 6B**). Our model further predicts that
419 after a fusion event, fission occurs when cells move apart from each other. In future studies,
420 it will be interesting to test if exogenous expression of TraAB in other bacteria with fluid OMs
421 facilitates OME. However, there are technical issues reconstituting the MYXO-CTERM
422 sorting pathway for TraA cell surface localization in a heterologous host (Sah *et al.*, 2020, Guo
423 *et al.*, 2025). Nevertheless, if successful, this method can be used in synthetic biology for
424 generating bacterial multicellular structures.

425 **Materials and methods**

426 **Bacterial strains, plasmids and growth conditions**

427 Vegetative *M. xanthus* cells were grown in liquid CYE medium (10 mM MOPS pH 7.6, 1%
428 (w/v) Bacto™ casitone (BD Biosciences), 0.5% yeast extract and 8 mM $MgSO_4$) at 32 °C, in
429 125-ml flasks with vigorous shaking, or on CYE plates that contains 1.5% agar.

430 Strains, plasmids, and primers used in this study are listed in Supplementary Table 1. To
431 create P_{pilA}-SS_{OM}-*PAmCherry* (pPC60), fragments of P_{pilA}-SS_{OM} and *PAmCherry* were PCR
432 amplified (Q5, New England Biolabs), and the resulting amplicons containing 25 bp
433 overhangs were ligated into the pSWU19 vector (linearized with EcoRI and XbaI) in
434 Gibson Assembly Master Mix (New England Biolabs). Construction of the SS_{IM}–
435 PAmCherry fusion was done following the published method (Wei *et al.*, 2011). This
436 construct was made by PCR amplification of genomic DNA with primers P_{pilA}-F2 and
437 SS_{IM}–mCherry-R (Table 1). The 5′ tail of the latter primer encodes 81 bp from MXAN_1176
438 that encode the N-terminal IM localization signal plus the downstream 10 amino acids
439 (CKDSDKKESM) for IM retention (Wei *et al.*, 2011). This PCR product was cloned to the
440 5′ end of PAmCherry at the XbaI site. Plasmids were verified by PCR, restriction enzyme
441 digestion, and if necessary, DNA sequencing. Verified plasmids were then electroporated
442 into *M. xanthus* cells and selected with appropriate antibiotics. The strains, plasmids and
443 primers used in this study are listed in **Table 1**.

444

445 **Table 1. Strains, plasmids, and primers used in this study.**

Strain name	Description	Source
DZ4469	DZ2 *pilA::tet,* Tc^R	(Vlamakis *et al.*, 2004)
DW1483	DK8601 (*aglQ1 pil*A*::tet*) Δ*traAB*, Tc^R	(Cao & Wall, 2017)
DW2279	DW1483 pPC44, Km^R, Tc^R	(Cao & Wall, 2019)
DW2285	DW1483 pPC49, Km^R, Tc^R	(Cao & Wall, 2019)
DW2302	DW8601 pPC60 Km^R, Tc^R	This study
BN360	DW8601 pBN-IMPAC Km^R, Tc^R	This study

Plasmid name	Description	Source
pPC60	P_{pilA}-*SS_{OM}-PAmCherry* in pSWU19, Km^R	This study
pPC41	P_{pilA}-*traA-gfp-traB* in pSWU19, Km^R	(Cao & Wall, 2019)
pPC44	P_{pilA}-*traA-mCherry-traB* in pSWU19, Km^R	(Cao & Wall, 2019)
pPC49	P_{pilA}-*traA-traB-gfp* in pSWU19, Km^R	(Cao & Wall, 2019)
pBN-IMPAC	P_{pilA}-*SS_{IM}-PAmCherry* in pSWU19, Km^R	This study

Primer name	Sequence (from 5' to 3')	Use
pSWU19-EcoRI-P_{pilA}-F	AGGAAACAGCTATGACCATGATTACGAATTCCGTCATGTTGGACGAGGT	pPC60
P_{pilA}-*SS_{OM}-PAmCherry*-R	GCCCTTGCTCACTCTAGAAGGAAACGAGCAACCG	pPC60
P_{pilA}-*SS_{OM}-PAmCherry*-F	GTTTCCTTCTAGAGTGAGCAAGGGCGAGGAG	pPC60
PAmCherry-XbaI-R	TGCATGCCTGCAGGTCGACTCTAGAAAGCTTTTACTTGTACAGCTCGTCCATGC	pPC60
P_{pilA}-F2	GGATCTAGATGCATGCGGCCGCGTCATGTTGGACGAGGTC	pBN-IMPAC
SS_{IM}-mCherry-R	CACATCTAGACATGGATTCCTTCTTGTCGGAGTCCTTGCAGGCGGTGAGGGTAAGGCAGAGGAGGACAGTCGTCAGGAATTGGGTCCGCATGGTGACTCTCCTCCGGGGGTCCTCAGAGAAGGTTG	pBN-IMPAC

446

447 **Light microscopy and image analysis**

448 For all imaging experiments, 5 ml cells or cell mixtures were spotted on a 1.5% (w/v) agar
449 pad containing 10 mM MOPS pH 7.6 and 8 mM $MgSO_4$. All microscopy images were
450 captured using an Andor iXon Ultra 897 EMCCD camera (effective pixel size 160 nm) on an
451 inverted Nikon Eclipse-Ti™ microscope with a 100× 1.49 NA TIRF objective. GFP and
452 mCherry were photobleached using the 488-nm and 561-nm lasers (0.5 kW/cm^2), respectively
453 at the stated frame rates. sptPALM was performed as previously described (Fu *et al.*, 2018).
454 *M. xanthus* cells were grown in CYE to OD_{600} around 1. PAmCherry was activated using a
455 405-nm laser (0.3 kW/cm^2), excited and imaged using a 561-nm laser (0.2 kW/cm^2). Images
456 were acquired at 67 Hz (15 ms/frame). For each sptPALM experiment, single PAmCherry

457 particles were localized in at least 100 individual cells from three biological replicates.
458 sptPALM and cell morphology data were analyzed as previously described using a MATLAB
459 (MathWorks) script (Fu *et al.*, 2018, Zhang *et al.*, 2023a, Zhang *et al.*, 2023b). Briefly, cells were
460 identified using differential interference contrast images. Single PAmCherry particles inside
461 of cells were fitted by a symmetric 2D Gaussian function; its center was assumed to be the
462 particle's position (Fu *et al.*, 2018). Particles in consecutive frames were considered to belong
463 to the same trajectory when they were within a user-defined distance of 320 nm (two pixels).
464 Sample trajectories were generated using the TrackMate plugin (Ershov *et al.*, 2022) in the
465 ImageJ suite (https://imagej.net). For simplicity, we considered all the mobile particles of
466 these proteins displaying typical diffusion and determined their D from a linear fit to the first
467 four points of the MSD using a simpler formula MSD = $4D\Delta t$ (Fu *et al.*, 2018, Lee *et al.*, 2016).
468 Error bars were the standard derivation of 1,000 bootstrap samples using the published
469 method (Morgenstein *et al.*, 2015).

470 **Cryo-EM**

471 Bacterial strains were grown overnight in CYE media with appropriate antibiotics,
472 incubated with shaking at 32 °C and 250 rpm to an optical density of OD_{600} 0.6. Cells were
473 collected by centrifugation at 5,000 rpm and room temperature for 3 min and
474 resuspended in CYE media to a final OD_{600} of 12. The cell suspension (3 μl) was applied
475 to C Flat-1.2/1.3 200 mesh copper grids (Electron Microscopy Sciences) that were glow
476 discharged for 30 s at 15 mA. Grids were plunge-frozen in liquid ethane with an FEI

477 Vitrobot Mark IV (Thermo Fisher Scientific) at 4 °C, 100% humidity with a waiting time
478 of 30 s, two-side blotting time of 2.5 - 3 s, and blotting force of 0. All subsequent grid
479 handling and transfers were performed in liquid nitrogen. Grids were clipped onto cryo-
480 FIB autogrids (Thermo Fisher Scientific). We used a Titan Krios G4 transmission electron
481 microscope (Thermo Fisher Scientific), equipped with a Gatan K3 direct electron detector
482 and a Gatan BioContinuum energy filter. Imaging was performed using a 15 eV slit width
483 on the energy filter to enhance image contrast. Micrographs were recorded in counted
484 mode at a nominal magnification of 30,000 x, using a dose rate of 14.65
485 electrons/pixel/second over a 2.6-second exposure, resulting in a total accumulated dose
486 of 50 electrons/$Å^2$. Low magnification images were taken at 6500 x with a pixel size of
487 1.39 nm.

488 **Acknowledgments**

489 This work was supported by the National Institutes of Health grants GM129000 to B. N. and

490 GM140886 to D.W.

491

492 **Movie captions**

493 **Movie S1.** TraA-GFP foci being photobleached. Time-lapse images were recorded at 67 Hz

494 and played at the same frame rate (real time).

495 **Movie S2.** Simultaneous photobleaching of TraA-mCherry (right) and TraB-GFP (left) in foci

496 between adjacent cells. Time-lapse images were recorded at 5 Hz and played at the same

497 frame rate (real time).

498 **Movie S3.** Diffusion of OM_{SS}-PAmCherry particles. Time-lapse images were recorded at 67

499 Hz and played at the same frame rate (real time).

500 **Movie S4.** Diffusion of IM_{SS}-PAmCherry particles. Time-lapse images were recorded at 67

501 Hz and played at the same frame rate (real time).

502 **Movie S5**. OME is bidirectional. The donor cell expresses OM_{SS}-PAmCherry (magenta) and

503 the recipient TraA-GFP (green). The particle was first transferred to the recipient and then

504 returned to the donor. Time-lapse images were recorded at 67 Hz and played at 7 frames/s,

505 about 1/10 speed of real time.

506 **Movie S6**. Serial cell-cell transfer of OM_{SS}-PAmCherry particle by OME. Donor cell expresses

507 OM_{SS}-PAmCherry (magenta) and the recipients TraA-GFP (green). Particle was serially

508 transferred, crossing three cell-cell boundaries. Time-lapse images were recorded at 67 Hz
509 and played at 7 frames/s, about 1/10 speed of real time.

510 **Movie S6**. TraAB foci do not function as OME conduits. Donor cell expresses OMss-
511 PAmCherry (magenta) and the recipients TraA-GFP (green). Two OMss-PAmCherry
512 particles transferred across cell boundaries, but not through the TraAB foci. Time-lapse
513 images were recorded at 67 Hz and played at 7 frames/s, about 1/10 speed of real time.

References

Balagam, R., Cao, P., Sah, G.P., Zhang, Z., Subedi, K., Wall, D., and Igoshin, O.A. (2021) Emergent Myxobacterial Behaviors Arise from Reversal Suppression Induced by Kin Contacts. *mSystems* **6**: e0072021.

Batsanov, S.S. (2001) Van der Waals Radii of Elements. *Inorganic Materials* **37**: 871-885.

Benn, G., Mikheyeva, I.V., Inns, P.G., Forster, J.C., Ojkic, N., Bortolini, C., Ryadnov, M.G., Kleanthous, C., Silhavy, T.J., and Hoogenboom, B.W. (2021) Phase separation in the outer membrane of *Escherichia coli*. *Proc Natl Acad Sci U S A* **118**.

Cao, P., Dey, A., Vassallo, C.N., and Wall, D. (2015) How Myxobacteria Cooperate. *J Mol Biol* **427**: 3709-3721.

Cao, P., and Wall, D. (2017) Self-identity reprogrammed by a single residue switch in a cell surface receptor of a social bacterium. *Proc Natl Acad Sci U S A* **114**: 3732-3737.

Cao, P., and Wall, D. (2019) Direct visualization of a molecular handshake that governs kin recognition and tissue formation in myxobacteria. *Nature communications* **10**: 3073.

Cao, P., and Wall, D. (2020) The Fluidity of the Bacterial Outer Membrane Is Species Specific: Bacterial Lifestyles and the Emergence of a Fluid Outer Membrane. *Bioessays* **42**: e1900246.

Cao, P., Wei, X., Awal, R.P., Muller, R., and Wall, D. (2019) A highly polymorphic receptor governs many distinct self-recognition types within the *Myxococcales* order. *mBio* **10**: 10.1128/mbio.02751-02718.

Cherrak, Y., Flaugnatti, N., Durand, E., Journet, L., and Cascales, E. (2019) Structure and Activity of the Type VI Secretion System. *Microbiol Spectr* **7**.

Dai, S., Sun, C., Tan, K., Ye, S., and Zhang, R. (2017) Structure of thrombospondin type 3 repeats in bacterial outer membrane protein A reveals its intra-repeat disulfide bond-dependent calcium-binding capability. *Cell Calcium* **66**: 78-89.

Dey, A., Vassallo, C.N., Conklin, A.C., Pathak, D.T., Troselj, V., and Wall, D. (2016) Sibling Rivalry in *Myxococcus xanthus* Is Mediated by Kin Recognition and a Polyploid Prophage. *Journal of Bacteriology* **198**: 994-1004.

Dey, A., and Wall, D. (2014) A genetic screen in *Myxococcus xanthus* identifies mutants that uncouple outer membrane exchange from a downstream cellular response. *J Bacteriol* **196**: 4324-4332.

Ducret, A., Fleuchot, B., Bergam, P., and Mignot, T. (2013) Direct live imaging of cell-cell protein transfer by transient outer membrane fusion in *Myxococcus xanthus*. *Elife* **2**: e00868.

Ershov, D., Phan, M.S., Pylvanainen, J.W., Rigaud, S.U., Le Blanc, L., Charles-Orszag, A., Conway, J.R.W., Laine, R.F., Roy, N.H., Bonazzi, D., Dumenil, G., Jacquemet, G., and Tinevez, J.Y. (2022) TrackMate 7: integrating state-of-the-art segmentation algorithms into tracking pipelines. *Nat Methods* **19**: 829-832.

Fu, G., Bandaria, J.N., Le Gall, A.V., Fan, X., Yildiz, A., Mignot, T., Zusman, D.R., and Nan, B. (2018) MotAB-like machinery drives the movement of MreB filaments during bacterial gliding motility. *Proc Natl Acad Sci U S A* **115**: 2484-2489.

Gong, Y., Zhang, Z., Zhou, X.W., Anwar, M.N., Hu, X.Z., Li, Z.S., Chen, X.J., and Li, Y.Z. (2018) Competitive Interactions Between Incompatible Mutants of the Social Bacterium Myxococcus xanthus DK1622. *Front Microbiol* **9**: 1200.

Grosberg, R.K., and Strathmann, R.R. (2007) The evolution of multicellularity: A minor major transition? *Annu Rev Ecol Evol S* **38**: 621-654.

559 Guo, T., Haft, D.H., and Wall, D. (2025) Myxosortase: an intramembrane protease that sorts
560 MYXO-CTERM proteins to the cell surface. *mBio*: e0406724.
561 Hodgkin, J., and Kaiser, D. (1977) Cell-to-cell stimulation of motility in nonmotile mutants of
562 *Myxococcus*. *Proc. Natl. Acad. Sci. USA* **74**: 2938-2942.
563 Jahn, R., Cafiso, D.C., and Tamm, L.K. (2024) Mechanisms of SNARE proteins in membrane
564 fusion. *Nat Rev Mol Cell Biol* **25**: 101-118.
565 Jumper, J., Evans, R., Pritzel, A., Green, T., Figurnov, M., Ronneberger, O., Tunyasuvunakool, K.,
566 Bates, R., Zidek, A., Potapenko, A., Bridgland, A., Meyer, C., Kohl, S.A.A., Ballard, A.J.,
567 Cowie, A., Romera-Paredes, B., Nikolov, S., Jain, R., Adler, J., Back, T., Petersen, S.,
568 Reiman, D., Clancy, E., Zielinski, M., Steinegger, M., Pacholska, M., Berghammer, T.,
569 Bodenstein, S., Silver, D., Vinyals, O., Senior, A.W., Kavukcuoglu, K., Kohli, P., and
570 Hassabis, D. (2021) Highly accurate protein structure prediction with AlphaFold. *Nature*
571 **596**: 583-589.
572 Lee, T.K., Meng, K., Shi, H., and Huang, K.C. (2016) Single-molecule imaging reveals modulation
573 of cell wall synthesis dynamics in live bacterial cells. *Nature communications* **7**: 13170.
574 Lorenzen, W., Bozhuyuk, K.A., Cortina, N.S., and Bode, H.B. (2014) A comprehensive insight
575 into the lipid composition of *Myxococcus xanthus* by UPLC-ESI-MS. *J Lipid Res* **55**: 2620-
576 2633.
577 Lucena, D., Mauri, M., Schmidt, F., Eckhardt, B., and Graumann, P.L. (2018) Microdomain
578 formation is a general property of bacterial membrane proteins and induces heterogeneity
579 of diffusion patterns. *BMC Biol* **16**: 97.
580 Morgenstein, R.M., Bratton, B.P., Nguyen, J.P., Ouzounov, N., Shaevitz, J.W., and Gitai, Z. (2015)
581 RodZ links MreB to cell wall synthesis to mediate MreB rotation and robust morphogenesis.
582 *Proc Natl Acad Sci U S A*.
583 Nan, B., Bandaria, J.N., Guo, K.Y., Fan, X., Moghtaderi, A., Yildiz, A., and Zusman, D.R. (2015)
584 The polarity of myxobacterial gliding is regulated by direct interactions between the
585 gliding motors and the Ras homolog MglA. *Proc Natl Acad Sci U S A* **112**: E186-193.
586 Nan, B., Bandaria, J.N., Moghtaderi, A., Sun, I.H., Yildiz, A., and Zusman, D.R. (2013) Flagella
587 stator homologs function as motors for myxobacterial gliding motility by moving in helical
588 trajectories. *Proc Natl Acad Sci U S A* **110**: E1508-1513.
589 Nudleman, E., Wall, D., and Kaiser, D. (2005) Cell-to-cell transfer of bacterial outer membrane
590 lipoproteins. *Science* **309**: 125-127.
591 Parry, B.R., Surovtsev, I.V., Cabeen, M.T., O'Hern, C.S., Dufresne, E.R., and Jacobs-Wagner, C.
592 (2014) The bacterial cytoplasm has glass-like properties and is fluidized by metabolic
593 activity. *Cell* **156**: 183-194.
594 Pathak, D.T., Wei, X., Bucuvalas, A., Haft, D.H., Gerloff, D.L., and Wall, D. (2012a) Cell contact-
595 dependent outer membrane exchange in myxobacteria: genetic determinants and
596 mechanism. *PLoS Genet* **8**: e1002626.
597 Pathak, D.T., Wei, X., Bucuvalas, A., Haft, D.H., Gerloff, D.L., and Wall, D. (2012b) Cell contact-
598 dependent outer membrane exchange in myxobacteria: genetic determinants and
599 mechanism. *PLoS Genet.* **8**: e1002626.
600 Pathak, D.T., Wei, X., Dey, A., and Wall, D. (2013) Molecular recognition by a polymorphic cell
601 surface receptor governs cooperative behaviors in bacteria. *PLoS Genet.* **9**: e1003891.
602 Perez-Burgos, M., Garcia-Romero, I., Jung, J., Valvano, M.A., and Sogaard-Andersen, L. (2019)
603 Identification of the lipopolysaccharide O-antigen biosynthesis priming enzyme and the O-
604 antigen ligase in *Myxococcus xanthus*: critical role of LPS O-antigen in motility and

605 development. *Mol Microbiol* **112**: 1178-1198.
606 Ramirez Carbo, C.A., Faromiki, O.G., and Nan, B. (2024) A lytic transglycosylase connects
607 bacterial focal adhesion complexes to the peptidoglycan cell wall. *Elife* **13**.
608 Rand, R.P., and Parsegian, V.A. (1984) Physical force considerations in model and biological
609 membranes. *Can J Biochem Cell Biol* **62**: 752-759.
610 Rassam, P., Copeland, N.A., Birkholz, O., Toth, C., Chavent, M., Duncan, A.L., Cross, S.J.,
611 Housden, N.G., Kaminska, R., Seger, U., Quinn, D.M., Garrod, T.J., Sansom, M.S., Piehler,
612 J., Baumann, C.G., and Kleanthous, C. (2015) Supramolecular assemblies underpin
613 turnover of outer membrane proteins in bacteria. *Nature* **523**: 333-336.
614 Rojas, E.R., Billings, G., Odermatt, P.D., Auer, G.K., Zhu, L., Miguel, A., Chang, F., Weibel, D.B.,
615 Theriot, J.A., and Huang, K.C. (2018) The outer membrane is an essential load-bearing
616 element in Gram-negative bacteria. *Nature* **559**: 617-621.
617 Sah, G.P., Cao, P., and Wall, D. (2020) MYXO-CTERM sorting tag directs proteins to the cell
618 surface via the type II secretion system. *Mol Microbiol* **113**: 1038-1051.
619 Sah, G.P., and Wall, D. (2020) Kin recognition and outer membrane exchange (OME) in
620 myxobacteria. *Curr Opin Microbiol* **56**: 81-88.
621 Shi, L., Shen, Q.T., Kiel, A., Wang, J., Wang, H.W., Melia, T.J., Rothman, J.E., and Pincet, F. (2012)
622 SNARE proteins: one to fuse and three to keep the nascent fusion pore open. *Science* **335**:
623 1355-1359.
624 Sinha, R., Ahmed, S., Jahn, R., and Klingauf, J. (2011) Two synaptobrevin molecules are sufficient
625 for vesicle fusion in central nervous system synapses. *Proc Natl Acad Sci U S A* **108**:
626 14318-14323.
627 Subedi, K., Roy, P.C., Saiz, B., Basile, F., and Wall, D. (2024) Cell-cell transfer of adaptation traits
628 benefits kin and actor in a cooperative microbe. *Proc Natl Acad Sci U S A* **121**:
629 e2402559121.
630 Sun, J., Rutherford, S.T., Silhavy, T.J., and Huang, K.C. (2022) Physical properties of the bacterial
631 outer membrane. *Nat Rev Microbiol* **20**: 236-248.
632 Tran, B.M., Punter, C.M., Linnik, D., Iyer, A., and Poolman, B. (2024) Single-protein Diffusion in
633 the Periplasm of *Escherichia coli*. *J Mol Biol* **436**: 168420.
634 van den Bogaart, G., Holt, M.G., Bunt, G., Riedel, D., Wouters, F.S., and Jahn, R. (2010) One
635 SNARE complex is sufficient for membrane fusion. *Nat Struct Mol Biol* **17**: 358-364.
636 Vassallo, C., Pathak, D.T., Cao, P., Zuckerman, D.M., Hoiczyk, E., and Wall, D. (2015) Cell
637 rejuvenation and social behaviors promoted by LPS exchange in myxobacteria. *Proc Natl*
638 *Acad Sci U S A* **112**: E2939-2946.
639 Vassallo, C.N., Cao, P., Conklin, A., Finkelstein, H., Hayes, C.S., and Wall, D. (2017) Infectious
640 polymorphic toxins delivered by outer membrane exchange discriminate kin in
641 myxobacteria. *Elife* **6**.
642 Vassallo, C.N., Troselj, V., Weltzer, M.L., and Wall, D. (2020) Rapid diversification of wild social
643 groups driven by toxin-immunity loci on mobile genetic elements. *ISME J* **14**: 2474-2487.
644 Vassallo, C.N., and Wall, D. (2016) Tissue repair in myxobacteria: A cooperative strategy to heal
645 cellular damage. *Bioessays* **38**: 306-315.
646 Vassallo, C.N., and Wall, D. (2019) Self-identity barcodes encoded by six expansive polymorphic
647 toxin families discriminate kin in myxobacteria. *Proc. Natl. Acad. Sci. USA* **116**: 24808-
648 24818.
649 Vlamakis, H.C., Kirby, J.R., and Zusman, D.R. (2004) The Che4 pathway of *Myxococcus xanthus*
650 regulates type IV pilus-mediated motility. *Mol Microbiol* **52**: 1799-1811.

651 Wall, D. (2014a) Molecular recognition in myxobacterial outer membrane exchange: functional,
652 social and evolutionary implications. *Mol Microbiol* **91**: 209-220.
653 Wall, D., (2014b) Social interactions mediated by outer membrane exchange. In: Myxobacteria:
654 Genomics, Cellular and Molecular Biology. Z. Yang, Higgs, P.I. (ed). Norfolk, UK: Caister
655 Academic Press, pp.
656 Wall, D., and Kaiser, D. (1998) Alignment enhances the cell-to-cell transfer of pilus phenotype.
657 *Proc Natl Acad Sci U S A* **95**: 3054-3058.
658 Wall, D., Wu, S.S., and Kaiser, D. (1998) Contact stimulation of Tgl and type IV pili in
659 *Myxococcus xanthus*. *J Bacteriol* **180**: 759-761.
660 Wei, X., Pathak, D.T., and Wall, D. (2011) Heterologous protein transfer within structured
661 myxobacteria biofilms. *Mol Microbiol* **81**: 315-326.
662 Weltzer, M.L., Guo, T., and Wall, D. (2025) Crosstalk between polymorphic toxin-immunity
663 systems involved in kin discrimination. *mBio* **0**: e00468-00425.
664 Yang, Z., Lux, R., Hu, W., Hu, C., and Shi, W. (2010) PilA localization affects extracellular
665 polysaccharide production and fruiting body formation in *Myxococcus xanthus*. *Mol*
666 *Microbiol* **76**: 1500-1513.
667 Zhang, H., Venkatesan, S., Ng, E., and Nan, B. (2023a) Coordinated peptidoglycan synthases and
668 hydrolases stabilize the bacterial cell wall. *GitHub*.
669 Zhang, H., Venkatesan, S., Ng, E., and Nan, B. (2023b) Coordinated peptidoglycan synthases and
670 hydrolases stabilize the bacterial cell wall. *Nature communications* **14**: 5357.

671